High Thermal Conductivity Materials

Subhash L. Shindé
Jitendra S. Goela
Editors

High Thermal Conductivity Materials

With 133 Illustrations

Springer

Editors

Subhash L. Shindé (Ed.)
Sandia National Labs.
P.O. Box 5800, MS 0603
Albuquerque, NM 87185
USA
slshind@sandia.gov

Jitendra S. Goela (Ed.)
Rohm and Haas Advanced Materials
185 New Boston Street
Woburn, MA 01801
USA
jgoela@rohmhaas.com

Library of Congress Cataloging-in-Publication Data
Shindé, Subhash L.
High thermal conductivity materials / Subhash L. Shindé, Jitendra S. Goela.
p. cm.
Includes bibliographical references and index.
ISBN 0-387-22021-6 (alk. paper)
1. Heat--Conduction. 2. Materials--Thermal properties. I. Shindé, Subhash L. Goela, Jitendra S. II. Title.

QC321.S44 2004
536′.2012—dc22 2004049159

ISBN-10: 0-387-22021-6 e-ISBN-: 0-387-25100-6

ISBN-13: 978-0387-22021-5

Printed on acid-free paper.

Printed in the United States of America. (SBA/Techset)

9 8 7 6 5 4 3 2 1

springeronline.com

In loving Memory of
Dr. Bhagwat Sahai Verma (1920–2005),
Retired Dean of Engineering,
Banaras Hindu University,
Varanasi, India

Preface

The demand for efficient thermal management has increased substantially over the last decade in every imaginable area, be it a formula 1 racing car suddenly braking to decelerate from 200 to 50 mph going around a sharp corner, a space shuttle entering the earth's atmosphere, or an advanced microprocessor operating at a very high speed. The temperatures at the hot junctions are extremely high and the thermal flux can reach values higher than a few hundred to a thousand watts/cm^2 in these applications. To take a specific example of the microelectronics area, the chip heat flux for CMOS microprocessors, though moderate compared to the numbers mentioned above have already reached values close to 100 W/cm^2, and are projected to increase above 200 W/cm^2 over the next few years. Although the thermal management strategies for microprocessors do involve power optimization through improved design, it is extremely difficult to eliminate "hot spots" completely. This is where high thermal conductivity materials find most of their applications, as "heat spreaders". The high thermal conductivity of these materials allows the heat to be carried away from the "hot spots" very quickly in all directions thereby "spreading" the heat. Heat spreading reduces the heat flux density, and thus makes it possible to cool systems using standard cooling solutions like finned heat sinks with forced air cooling. A quick review of the available information indicates that the microprocessors heat fluxes are quickly reaching the 100 W/cm^2 values, which makes it very difficult to use conventional air cooling (see for example, "Thermal challenges in microprocessor testing", by P. Tadayan et al. Intel Technology Journal, Q3, 2000, and Chu, R., and Joshi, Y., Eds. "NEMI Technology Roadmap, National Electronics Manufacturing Initiative", Herndon, VA, 2002).

One approach to address this problem is to design and develop materials with higher thermal conductivities. This is possible by developing a detailed understanding of the thermal conduction mechanisms in these materials and studying how the processing and resulting microstructures affect their thermal properties. These aspects are the subject matter of review in this book.

We have chosen to review our current understanding of the conduction mechanisms in the high thermal conductivity materials, various techniques to measure the thermal conductivity accurately, and the processing and thermal conduction properties of a few candidate high thermal conductivity materials. This is by no means an exhaustive review, but the chapters authored by internationally known experts should provide a good review of the status of their field and form a sound basis for further studies in these areas.

The eight chapters in this book are arranged to provide a coherent theme starting from theory to understanding of practical materials, so a scientist would be able to optimize properties of these materials using basic concepts. In Chapter 1, Srivastava covers the thermal conduction mechanisms in nonmetallic solids in some detail. The thermal conductivity expression derived is used to provide guidelines for choosing high thermal conductivity materials. Thermal conductivity results for various materials including diamond, carbon nanotubes, and various other forms of carbon are presented. The results are also extended to polycrystalline, and low dimensional systems. In Chapter 2, Morelli deals with the thermal conductivity of materials near their Debye temperatures. It also compares the results of a simple model to experimental data from various classes of crystal structures. Ashegi et al. discusses accurate characterization of thermal conductivity of various materials in Chapter 3. They review various thermal conductivity measurement techniques available to a researcher in detail, and also recommend techniques particularly suitable for high thermal conductivity materials like AlN, SiC, and diamond. In Chapter 4. Fournier reviews an elegant technique, perfected by her group, for measuring thermal conductivity on a very small spatial scale in heterogeneous materials. It is believed that this technique would be very important when evaluating thermal performance of complex systems. Virkar et al. provides the current status of the understanding of processing, and resultant thermal conductivity of aluminum nitride ceramics in Chapter 5. This chapter lays out the thermodynamic foundation for processing that will result in oxygen impurity removal from AlN, and thus increase its thermal conductivity. We hope that general application of these concepts will help researchers optimize thermal conductivity of a host of material systems. In Chapters 6 and 7, Goela et al. describe the details of CVD-SiC, and diamond materials processing and their properties. Here again the inter-relationship between the microstructure development through processing, and its effect on thermal conductivity is presented. Finally, in Chapter 8, Kwon et al. describe theoretical and experimental aspects of the thermal transport properties of carbon nanotubes. The strong carbon atom network in these novel materials lead not only to very unusual mechanical and electrical properties, but also to high thermal conductivity along the tube axis. We hope that the concepts described in these chapters will survive the test of time, and launch many curious scientists into their own forays in this field of highly interesting materials and their properties.

The editors would like to thank all the authors for their time and effort and the Springer, New York staff for their highly professional handling of the production of this volume. Subhash L. Shindé would like to acknowledge his colleagues for their critical review of these manuscripts.

Subhash L. Shindé
Jitendra S. Goela
July, 2005

Contents

Preface ..... **vii**

Contributors ..... **xvii**

1 Lattice Thermal Conduction Mechanism in Solids **1**
G.P. Srivastava
1.1 Introduction 1
1.2 Theory of Thermal Conductivity 2
1.2.1 Green-Kubo Linear-Response Theory 3
1.2.2 Variational Principles 4
1.2.3 Relaxation-Time Approaches 6
1.3 Phonon-Dispersion Relations 8
1.3.1 Three-Dimensional Materials 8
(i) Diamond 8
(ii) β-AlN 9
(iii) α-AlN 10
1.3.2 Graphite, Graphene, and Nanotubes 11
(i) Graphite 11
(ii) Graphene 12
(iii) Nanotubes 14
1.3.3 Debye's Isotropic Continuum Model 15
1.4 Phonon Relaxation Times 16
1.4.1 Extrinsic Relaxation Times 17
(i) Boundary Scattering 17
(ii) Scattering from Static Point Imperfections 17
(iii) Scattering from Imperfection Aggregates, Dislocations, Stacking Faults, and Grain Boundaries ... 17
1.4.2 Intrinsic Relaxation Times 18
(i) Interactions Involving Acoustic Phonons 19
(ii) Role of Optical Phonons 20

1.5 Conductivity of Single Crystals 21
1.5.1 Simplified Conductivity Integral 21
1.5.2 Temperature Variation of Conductivity 22
1.5.3 High-Thermal-Conductivity Materials 22
1.5.4 Conductivity of Diamond-Structure Single Crystals 23
1.6 Conductivity of Polycrystalline Solids 25
1.7 Conductivity of Low-Dimensional Solids 26
1.7.1 Superlattices 26
1.7.2 Semiconductor Quantum Wells and Wires 27
1.7.3 Graphite, Graphene, Carbon Nanotubes, and Fullerenes 29
1.8 Summary 33

2 High Lattice Thermal Conductivity Solids 37
Donald T. Morelli and Glen A. Slack
2.1 Introduction: The Importance of Thermal Conductivity 37
2.2 Simple Model of the Magnitude of Lattice Heat Conduction in Solids 39
2.2.1 Normal Modes of Vibrations of a Lattice 39
2.2.2 Normal and Umklapp Phonon-Scattering Processes 42
2.2.3 Relaxation-Time Approximation 43
2.2.4 Callaway Model 43
2.2.5 Thermal Conductivity Near the Debye Temperature . . . 44
2.2.6 Extension to More Complex Crystal Structures and Criteria for High Thermal Conductivity 44
2.3 Materials with High Lattice Thermal Conductivity 45
2.3.1 Rocksalt, Diamond, and Zincblende Crystal Structures 45
2.3.2 Wurtzite Crystal Structure 48
2.3.3 Silicon Nitride and Related Structures 50
2.3.4 Icosahedral Boron Compounds 54
2.3.5 Graphite and Related Materials 54
2.4 Thermal Conductivity of Wide-Band-Gap Semiconductors: Silicon Carbide, Aluminum Nitride, and Gallium Nitride 57
2.5 Isotope Effect in High Lattice Thermal Conductivity Materials 62
2.6 Summary 64

3 Thermal Characterization of the High-Thermal-Conductivity Dielectrics 69
Yizhang Yang, Sadegh M. Sadeghipour, Wenjun Liu, Mehdi Asheghi and Maxat Touzelbaev
3.1 Introduction 69
3.2 Microstructure of High-Thermal-Conductivity Dielectrics and Its Relevance to Thermal Transport Properties 72

3.2.1 CVD Diamond 72
3.2.2 CVD Silicon Nitride (Si_3N_4) 75
3.2.3 Aluminum Nitride (AlN) 75
3.2.4 CVD Silicon Carbide (SiC) 77
3.3 Overview of the Measurement Techniques 77
3.3.1 The Heating and Thermometry Techniques 78
3.3.2 Measurement Time Scale 79
3.3.3 Impact of Geometry on Thermal Property Measurements in the Transient Techniques 80
3.4 Steady-State Techniques 83
3.4.1 The Heated Suspended Bar Technique 85
3.4.2 The Film-on-Substrate Technique 88
3.4.3 The DC Heated Suspended Membrane 91
3.4.4 The Comparator Method 95
3.5 Frequency-Domain Techniques 97
3.5.1 The Ångström Thermal Wave Technique 98
3.5.2 The Modified Calorimetric Method 99
3.5.3 The High-Thermal-Conductivity Films on the Low-Thermal-Conductivity Substrates 101
3.5.4 Thermal Characterization of the Anisotropic Silicon-Nitride Substrates 102
3.5.5 Thermal Characterization of the AlN Substrates with Spatially Variable Thermal Conductivity 104
3.5.6 The Mirage Technique 106
3.6 Time-Domain Techniques 107
3.6.1 The Laser Heating Method 107
3.6.2 The Joule Heating Method 111
3.6.3 The Thermal Grating Technique 111
3.7 Summary 112

4 Thermal Wave Probing of High-Conductivity Heterogeneous Materials 119
Danièle Fournier
4.1 Introduction 119
4.2 Thermal Parameter Determination with a Photothermal Experiment 120
4.2.1 Photothermal Experiment Principle 120
4.2.2 Plane and Spherical Thermal Waves 120
4.2.3 Thermal Conductivity, Thermal Diffusivity, and Thermal Effusivity 122
4.2.4 Thermal Waves and Photothermal Setups 122
4.2.5 Analysis of the Experimental Data 123
4.2.5.1 Bulk Sample 123
4.2.5.2 Influence of the Sample Thickness 123

4.2.5.3 Absorbing and Reflected Layer Deposited on Top of the Sample . . . 125
4.2.5.4 Multilayered Samples . . . 126
4.3 Photothermal Experiments on Complex Materials at Millimeter Scale . . . 128
4.3.1 Determination of the Thermal Diffusivity with the Mirage Experiment . . . 128
4.3.2 Thermal Diffusivity Determination on CVD Diamond Samples . . . 130
4.3.3 Aluminium Nitride Ceramics . . . 130
4.3.4 Silicon Nitride Ceramics . . . 132
4.3.5 Thermal Heterogeneïty Evidence on Diamond Samples . 132
4.4 Photothermal Experiment at Microscopic Scale . . . 133
4.4.1 Photothermal Microscope . . . 133
4.4.2 Thermal Diffusivity Measurement at a Single Grain Scale . . . 134
4.4.2.1 AlN Ceramics . . . 134
4.4.2.2 Si_3N_4 Ceramics . . . 135
4.4.3 Photothermal Imaging . . . 136
4.4.4 Thermal Barrier Evidence on AlN Ceramics . . . 136
4.4.5 Very Thin Layer Thermal Property Determination . . . 138
4.4.5.1 Thermal Diffusivity Determination of the Substrate . . . 139
4.4.5.2 Determination of the YbaCuO Layer Thermal Diffusivity and of the Thermal Interface Resistance . . . 141
4.5 Conclusion . . . 141

5 Fabrication of High-Thermal-Conductivity Polycrystalline Aluminium Nitride: Thermodynamic and Kinetic Aspects of Oxygen Removal . . . 143
Anil V. Virkar and Raymond A. Cutler
5.1 Theoretical Basis . . . 143
5.2 Procedures for the Fabrication of High-Thermal-Conductivity Aluminum Nitride Ceramics . . . 146
5.3 Phase Equilibria, Sintering, and Thermodynamic Considerations . . . 148
5.3.1 Free Energies of Formation and the Activity of Al_2O_3 . . 151
5.3.2 Thermodynamics of Oxygen Removal and the Analysis of Thermal Conductivity . . . 154
5.3.3 Kinetics of Oxygen Removal and Microstructural Changes . . . 155
5.3.4 Long-Term Annealing and Microstructural Changes 161
5.4 Summary . . . 164

6 High-Thermal-Conductivity SiC and Applications 167
J.S. Goela, N.E. Brese, L.E. Burns, and M.A. Pickering
6.1 Introduction 167
6.2 CVD-SiC Process 169
6.3 Properties of CVD-SiC 173
6.3.1 Thermal Properties 177
6.3.1.1 Thermal Conductivity and Specific Heat 177
6.3.1.2 Thermal Expansion Coefficient 181
6.3.1.3 Thermal Shock Resistance 182
6.3.2 Mechanical Properties 182
6.3.3 Electrical Properties 185
6.3.4 Optical Properties 185
6.4 High-Thermal-Conductivity Applications 189
6.4.1 Thermal Management and Semiconductor Processing Applications 189
6.4.2 Optics and Wear Applications 191
6.5 Summary and Conclusions 194

7 Chemical-Vapor-Deposited Diamond for High-Heat-Transfer Applications 199
J.S. Goela and J.E. Graebner
7.1 Introduction 199
7.2 Diamond Synthesis by CVD 202
7.2.1 Postdeposition Processing 206
7.3 Properties of CVD Diamond 208
7.3.1 Thermal Conductivity of Diamond 209
7.3.1.1 Local Thermal Conductivity 211
7.3.1.2 Thermal Conduction Near Diamond-Substrate Interface. 216
7.3.1.3 Thermal Conductivity of Isotopically Enriched Diamond 218
7.3.2 Thermal Shock Resistance 219
7.4 High-Thermal-Conductivity Applications 220
7.4.1 Thermal Management Applications 221
7.4.2 Optics and Other Applications 221
7.5 Summary and Conclusions 222

8 Unusually High Thermal Conductivity in Carbon Nanotubes 227
Young-Kyun Kwon and Philip Kim
8.1 Introduction 227
8.2 Theory of Energy Conduction in Carbon Nanotubes 228
8.2.1 Phonons in Carbon Nanotubes 231
8.2.2 Computational Methods 237

8.2.2.1 Direct Molecular Dynamics Approach Based on Velocity Rescaling . . . 238
8.2.2.2 Equilibrium Molecular Dynamics Simulations Based on the Green-Kubo Formalism . . . 240
8.2.2.3 Nonequilibrium Molecular Dynamics Simulations Based on the Green-Kubo Formalism . . . 241
8.2.3 Thermal Conductivity of Carbon Nanotubes . . . 242
8.3 Experiments of Thermal Conduction in Carbon Nanotubes . . . 246
8.3.1 Bulk Thermal-Conductivity Measurements of Carbon Nanotubes . . . 247
8.3.2 Experimental Method for the Mesoscopic Thermal Transport Measurement . . . 252
8.3.3 Thermal Conductivity of Multiwalled Nanotubes . . . 257
8.4 Summary and Future Work . . . 262

Index . . . 267

Contributors

Editors:
Subhash L. Shindé
Sandia National Labs
P.O. Box 5800, MS 0603
Albuquerque, NM 87185
USA
slshind@sandia.gov

Jitendra S. Goela
Rohm and Haas Advanced Materials
185 New Boston Street
Woburn, MA 01801, USA
jgoela@rohmhaas.com

Chapter 1
Lattice Thermal Conduction
Mechanism in Solids

Gyaneshwar P. Srivastava
School of Physics
University of Exeter
Stocker Road, Exeter EX4 4QL,
United Kingdom
gps@excc.ex.ac.uk

Chapter 2
High Lattice Thermal Conductivity
Solids

Donald T. Morelli
Materials Group, Delphi Corporation
Research Labs.
Shelby Township, MI, 48315, USA
donald.t.morelli@delphi.com

Glen A. Slack
Rensselaer Polytechnic Institute (RPI)
110 8th St., Troy, NY 12180, USA

Chapter 3
Thermal Characterization of the
High-Thermal-Conductivity Dielectrics

Yizhang Yang
Mechanical Engineering Department
Carnegie Mellon University
5000 Forbes Avenue
Pittsburgh, PA 15213, USA
yizhangy@andrew.cmu.edu

Sadegh M. Sadeghipour
Mechanical Engineering Department
Carnegie Mellon University
5000 Forbes Avenue
Pittsburgh, PA 15213, USA
sms@andrew.cmu.edu

Wenjun Liu
Mechanical Engineering Department
Carnegie Mellon University
5000 Forbes Avenue
Pittsburgh, PA 15213, USA
wenjunl@andrew.cmu.edu

Mehdi Asheghi
Mechanical Engineering Department
Carnegie Mellon University
5000 Forbes Avenue
Pittsburgh, PA 15213, USA
masheghi@andrew.cmu.edu

Maxat Touzelbaev
Advanced Micro Devices
3625, Peterson Way, MS 58
Santa Clara, CA 95054, USA
maxat.touzelbaev@amd.com

Chapter 4
Thermal Wave Probing of High-Conductivity Heterogeneous Materials

Danièle Fournier
Laboratoire UPR A005 du CNRS
ESPCI, 10 rue Vauquelin 75005 Paris, France
fournier@optique.espci.fr

Chapter 5
Fabrication of High-Thermal-Conductivity Polycrystalline Aluminum Nitride: Thermodynamic and Kinetic Aspects of Oxygen Removal

Anil V. Virkar
Materials Science and Engineering
Energy & Mineral Research Office
122 S Central Campus Drive,
Room 304
University of Utah
Salt Lake City, UT 84112, USA
anil.virkar@m.cc.utah.edu

Raymond A. Cutler
Ceramatec, Inc.
2425 S. 900 W.
Salt Lake City, UT 84119, USA
cutler@ceramatec.com

Chapter 6
High-Thermal-Conductivity SiC and Applications

J.S. Goela
Rohm and Haas Advanced Materials
185 New Boston Street
Woburn, MA 01801, USA
jgoela@rohmhaas.com

N.E. Brese
Rohm and Haas Electronic Materials
272 Buffalo Ave.
Freeport, NY 11520, USA
NBrese@rohmhaas.com

L.E. Burns
Formerly at Rohm and Haas
Advanced Materials
185 New Boston Street
Woburn, MA 01801, USA
leeburns@shore.net

M.A. Pickering
Rohm and Haas Advanced Materials
185 New Boston Street
Woburn, MA 01801, USA
mpickering@rohmhaas.com

Chapter 7
Chemical-Vapor-Deposited Diamond for High-Heat-Transfer Applications

J.S. Goela
Rohm and Haas Advanced Materials
185 New Boston Street
Woburn, MA 01801, USA
jgoela@rohmhaas.com

J.E. Graebner
Formerly at
TriQuint Optoelectronics
9999 Hamilton Blvd.
Breinigsville, PA 18031, USA
jegraebner@mailaps.org

Chapter 8
Unusually High Thermal Conductivity in Carbon Nanotubes

Young-Kyun Kwon
Department of Physics
University of California
Berkeley, CA 94720, USA
ykkwon@civet.berkeley.edu

Philip Kim
Department of Physics,
Columbia University
New York, NY 10027, USA
pkim@phys.columbia.edu

1

Lattice Thermal Conduction Mechanism in Solids

G.P. Srivastava

The theory of lattice thermal conductivity of nonmetallic solids is presented. After discussing the fundamental issues, the kinetic-theory expression for the conductivity, based on the concept of single-mode phonon relaxation time, is developed in some detail, emphasizing the role of phonon dispersion relations and phonon scattering rates. The theory presented contains only one possible adjustable parameter, *viz.* Grüneisen's anharmonic coefficient γ. The simplified intrinsic conductivity expression, within the high-temperature approximation, is used to derive a set of rules for choosing high-thermal-conductivity materials. The theory is extended to provide a discussion on the conductivity of solids in polycrystalline and low-dimensional forms. Thermal conductivity results of quantum wells, quantum wires, and different solid forms of carbon, *viz.* diamond, graphite, graphene, nanotubes, and fullerenes, are presented and discussed.

1.1 Introduction

One of the fundamental properties of solids is their ability to conduct heat. This property is usually quantified in terms of the thermal conductivity coefficient $\mathcal{K}$, which is defined through the macroscopic expression for the rate of heat energy flow per unit area $\mathbf{Q}$ normal to the gradient ∇T

$$\mathbf{Q} = -\mathcal{K}\ \nabla T. \tag{1.1}$$

Understanding and controlling the thermal conductivity $\mathcal{K}$ of semiconductors plays an important part in the design of power-dissipating devices. For example, power transistors, solar cells under strong sunlight, diodes, transistors, and semiconductor lasers sustain large internal power dissipation, and a high thermal conductivity of the device material can help transfer this energy to a heat sink. On the other hand, a low thermal conductivity of semiconductor alloys helps increase the figure of merit of thermoelectric devices.

In nonmetals heat is conducted by phonons, quanta of atomic vibrational modes. The thermal conductivity of a hypothetical crystal is infinite at all temperatures if it is considered to be infinitely large, is isotopically pure, has no imperfections, and is characterized by purely harmonic atomic vibrations. Within the pure harmonic limit a phonon is infinitely long-lived, characterized with its frequency $\omega(\mathbf{q}s)$ for wave vector $\mathbf{q}$ and polarization index s (longitudinal L or transverse T). Thus, on the application of a temperature gradient, phonons of a purely harmonic crystal would transport all heat from the hot end to the cold end. In other words, the thermal conductivity of a purely harmonic crystal would be infinite at all temperatures. However, real solids are of finite size, contain defects, and exhibit anharmonicity in atomic vibrations. These realities limit the lifetime of phonons, rendering finite values of thermal conductivity. Experimental measurements indicate strong temperature dependence of the conductivity.

Intrinsic phonon-phonon interactions, caused by anharmonicity at finite temperatures, are inelastic in nature. This makes the concept of phonon lifetime an intrinsically difficult, if not impossible, concept to comprehend and thus evaluate theoretically. Thus, it is not usually possible to obtain an exact expression for $\mathcal{K}$. In this chapter we will discuss the progress made toward developing plausible theoretical models for lattice thermal conduction mechanisms in nonmetallic solids. It will be pointed out that whatever theory is adopted for deriving an expression for the thermal conductivity of a nonmetallic solid, its numerical evaluation requires an accurate knowledge of two essential inputs: (1) phonon-dispersion relation, and (2) relevant phonon-scattering mechanisms (to construct the phonon-scattering operator or to derive the phonon relaxation time). After a brief discussion of these aspects, we will follow a simple relaxation-time scheme, based on an isotropic continuum model, to discuss the theory of thermal conduction in crystalline, polycrystalline, and low-dimensional forms of nonmetals. The high-temperature expression for the conductivity will be used to derive a set of rules for choosing high-thermal-conductivity materials. Thermal conductivity results for the various solid forms of carbon, *viz.* diamond, graphite, graphene, nanotubes, and fullerene, will be presented and discussed.

1.2 Theory of Thermal Conductivity

Let us consider a crystal with N_0 unit cells, each of volume Ω. Let us also identify a phonon with its wave vector $\mathbf{q}$, polarization index s, frequency $\omega(\mathbf{q}s)$, and group velocity $c_s(\mathbf{q})$. The heat current $\mathbf{Q}$ can be expressed by including contributions from phonons in all possible modes

$$\mathbf{Q} = \frac{1}{N_0\Omega}\sum_{\mathbf{q}s}\hbar\omega(\mathbf{q}s)n_{\mathbf{q}s}c_s(\mathbf{q}). \tag{1.2}$$

The quantity $n_{\mathbf{q}s}$, which is explained later, assumes its equilibrium value $\bar{n}_{\mathbf{q}s}$ characterized by the crystal temperature T. In the presence of a temperature gradient across the crystal we can express

$$n_{\mathbf{q}s} = \bar{n}_{\mathbf{q}s} + \delta n_{\mathbf{q}s}, \tag{1.3}$$

where $\delta n_{\mathbf{q}s}$ indicates deviation from the equilibrium value. Clearly, then, the heat current is governed by $\delta n_{\mathbf{q}s}$, so that Eq. (1.2) can be reexpressed as

$$\mathbf{Q} = \frac{1}{N_0\Omega}\sum_{\mathbf{q}s}\hbar\omega(\mathbf{q}s)\delta n_{\mathbf{q}s}c_s(\mathbf{q}). \tag{1.4}$$

The deviation quantity $\delta n_{\mathbf{q}s}$, which is significantly controlled by crystal anharmonicity, particularly at high temperatures, is in general unknown.

Microscopic theories of lattice thermal conductivity attempt to address the quantity $\delta n_{\mathbf{q}s}$. Two fundamentally different approaches have been developed: (1) linear-response methods based on the Green-Kubo formalism and (2) methods based on solving the phonon Bolzmann equation. A detailed discussion of these theoretical methods can be found in the book by Srivastava [1]. Here we will briefly outline the fundamental concepts underlying these approaches.

1.2.1 Green-Kubo Linear-Response Theory

The Green-Kubo formalism is rooted in quantum statistics. It begins by expressing Eq. (1.4) as

$$\mathcal{K} = \frac{k_{\mathrm{B}}T^2N_0\Omega}{3}\,\Re\int_0^\infty\langle\mathbf{Q}(0)\cdot\mathbf{Q}(t)\rangle\mathrm{d}t \tag{1.5}$$

$$= \frac{\hbar^2}{3N_0\Omega k_{\mathrm{B}}T^2}\,\Re\int_0^\infty\mathrm{d}t\sum_{\mathbf{q}s\mathbf{q}'s'}\omega(\mathbf{q}s)\omega(\mathbf{q}'s')\mathbf{c}_s(\mathbf{q})\cdot\mathbf{c}'_s(\mathbf{q}')\mathcal{C}_{\mathbf{q}s\mathbf{q}'s'}(t), \tag{1.6}$$

where

$$\mathcal{G}(t) \equiv \langle\delta n_{\mathbf{q}s}(0)\delta n_{\mathbf{q}'s'}(t)\rangle \equiv \mathcal{C}_{\mathbf{q}s\mathbf{q}'s'}(t) \tag{1.7}$$

is a *correlation function*. The quantity $n_{\mathbf{q}s}$ is regarded as the number-density operator for phonons in mode $\mathbf{q}s$ in the Heisenberg representation:

$$n_{\mathbf{q}s}(t) = a^\dagger_{\mathbf{q}s}(t)a_{\mathbf{q}s}(t), \tag{1.8}$$

where $a^\dagger_{\mathbf{q}s}$ and $a_{\mathbf{q}s}$ are the creation and annihilation operators, respectively.

As $\delta n_{\mathbf{q}s}$ is generally unknown, an exact evaluation of $\mathcal{G}$ is not possible. Approximate expressions for $\mathcal{G}$ can be derived by employing several theoretical techniques, such as the Zwangiz–Mori projection operator method, double-time Green function method, and imaginary-time Green function method. The first two of these methods have been described in the book by Srivastava [1], to which the interested reader is referred for details.

1.2.2 Variational Principles

In applying variational principles for deriving approximate expressions for $\mathcal{K}$, the quantity $n_{\mathbf{q}s}$ is considered as a distribution function $n_{\mathbf{q}s}(\mathbf{r},t)$ that measures the occupation number of phonons $(\mathbf{q}s)$ in the neighborhood of a point $\mathbf{r}$ in space at time t. In the absence of an external temperature gradient, the thermal average of the distribution function is given by the Bose-Einstein expression

$$\bar{n}_{\mathbf{q}s} = \frac{1}{\exp[\hbar\omega(\mathbf{q}s)/k_{\mathrm{B}}T]-1}. \tag{1.9}$$

In the steady state of heat flow through a crystal, the total time rate of change of the distribution function $n_{\mathbf{q}s}(\mathbf{r},t)$ satisfies the Boltzmann equation

$$\left.\frac{\partial n_{\mathbf{q}s}}{\partial t}\right|_{\mathrm{diff}} + \left.\frac{\partial n_{\mathbf{q}s}}{\partial t}\right|_{\mathrm{scatt}} = 0, \tag{1.10}$$

where the first term represents *diffusion* (i.e., variation from point to point) of $n_{\mathbf{q}s}(\mathbf{r},t)$ through the solid, and the second term represents the rate of change of $n_{\mathbf{q}s}(\mathbf{r},t)$ due to possible phonon-scattering processes. Noting that in equilibrium $\partial\bar{n}_{\mathbf{q}s}/\partial t = 0$, a canonical form of the linearized phonon Boltzmann equation reads

$$-\mathbf{c}_s(\mathbf{q})\cdot\nabla T\frac{\partial\bar{n}_{\mathbf{q}s}}{\partial T} = -\left.\frac{\partial n_{\mathbf{q}s}}{\partial t}\right|_{\mathrm{scatt}}. \tag{1.11}$$

This form of the phonon Bolzmann equation can be written in a standard form

$$X^s_{\mathbf{q}} = \sum_{\mathbf{q}'s'} P^{ss'}_{\mathbf{q}\mathbf{q}'}\psi^{s'}_{\mathbf{q}'}, \tag{1.12}$$

where $X^s_{\mathbf{q}}$ is a measure of inhomogeneity caused by the application the of the temperature gradient, $P^{ss'}_{\mathbf{q}\mathbf{q}'}$ is an element of the phonon-scattering operator, and $\psi^s_{\mathbf{q}} \equiv \psi_{\mathbf{q}s}$ is a function that measures the deviation quantity $\delta n_{\mathbf{q}s}$ defined as follows

$$n_{\mathbf{q}s} = \frac{1}{\exp[\hbar\omega(\mathbf{q}s)/k_{\mathrm{B}}T - \psi_{\mathbf{q}s}]-1} \tag{1.13}$$

$$\simeq \bar{n}_{\mathbf{q}s} + \psi_{\mathbf{q}s}\bar{n}_{\mathbf{q}s}(\bar{n}_{\mathbf{q}s}+1). \tag{1.14}$$

Using Eqs. (1.4) and (1.12), the following expression for the thermal conductivity can be obtained

$$\mathcal{K} = \frac{k_{\mathrm{B}}T^2}{N_0\Omega \mid \nabla T \mid^2}\sum_{\mathbf{q}s}\psi^s_{\mathbf{q}}X^s_{\mathbf{q}}. \tag{1.15}$$

This expression cannot be evaluated exactly, as the anharmonic contribution to the deviation function $\psi_{\mathbf{q}s}$ is generally unknown. An effort to express ψ in terms of the inverse scattering operator P^{-1} would remain unsuccessful, as

the full set of eigenvalues and eigenvectors of the operator P is not known [2]. Obtaining an approximation for Eq. (1.15) thus becomes a cherished topic of the variational method.

In a simple variational approach the deviation function is expressed as

$$\psi_{\mathbf{q}s} = \phi_{\mathbf{q}s} + \delta\phi_{\mathbf{q}s} \tag{1.16}$$

and the semidefinite property of the operator P is expressed as

$$(\delta\boldsymbol{\phi}, P\delta\boldsymbol{\phi}) \geq 0. \tag{1.17}$$

A simple form of variational trial function $\phi_{\mathbf{q}s}$ can be chosen as

$$\phi_{\mathbf{q}s} = \mathbf{q} \cdot \mathbf{u}, \tag{1.18}$$

where $\mathbf{u}$ is some constant vector parallel to the applied temperature gradient. This choice for a variational trial function has been made from the momentum-conserving property of anharmonic phonon normal (N) processes [3, 4] (also see Sect. 1.4.2). With this choice of the trial function a lower bound $\mathcal{K}_0^<$ for the exact conductivity coefficient $\mathcal{K}$ can be derived [5, 6]: $\mathcal{K}_0^< \leq \mathcal{K}$,

$$\mathcal{K}_0^< = \frac{(\boldsymbol{\phi}, \mathbf{X})}{(\boldsymbol{\phi}, P\boldsymbol{\phi})^2}, \tag{1.19}$$

where $(\mathbf{f}, \mathbf{g}) = \sum_{\mathbf{q}s} f_{\mathbf{q}s} g_{\mathbf{q}s}$ is implied. The Ziman bound $\mathcal{K}_0^<$ can be improved, i.e., brought closer to $\mathcal{K}$, by employing a more general trial function [7], such as one made as a linear combination of a few simple trial functions in powers of q: $\boldsymbol{\phi} = \sum_{n=1}^{N} \alpha_n \boldsymbol{\phi}_n$.

The ubiquitous simple form of the variational principle just described can be extended to take the form of *complementary variational principles* [8]. To develop such principles the phonon scattering operator P is split in the form $P = \mathcal{L} + \mathcal{T}^*\mathcal{T}$, such that $\mathcal{L}^{-1}$ exists and $\mathcal{T}^*$ is the conjugate of $\mathcal{T}$. Using the split form of P the phonon Boltzmann equation in Eq. (1.12) can be expressed in a canonical Euler-Lagrange form, from which an upper and a lower bound on $\mathcal{K}$ can be derived. As an alternative to using the Euler-Lagrange variational principles, the upper and lower bounds on $\mathcal{K}$ can also be derived by applying Schwarz's inequality based on the positive semidefinite nature of P and $(P\mathcal{L}^{-1} - \hat{I})$: $(\mathbf{f}, P\mathbf{f}) \geq 0$ and $(\mathbf{f}, (P\mathcal{L}^{-1} - \hat{I})\mathbf{f}) \geq 0$ for any admissible vector function $\mathbf{f}$. Using these ideas, monotonically convergent sequences of lower bounds $\{\mathcal{K}_m^<\}, m = 0, 1, 2, \ldots$ [9] and upper bounds $\{\mathcal{K}_n^>\}, n = 1, 3, 5, \ldots$ [10] for thermal conductivity can be derived.

While the derivation and application of the method of complementary variational principles are somewhat involved, it is easy to appreciate their achievement. Consider a pair of complementary bounds: an upper bound $\mathcal{K}_n^>$ and a lower bound $\mathcal{K}_m^<$, with suitably chosen large values of m and n. From these two bounds we can define a narrow window $\Delta_{m,n} = \mathcal{K}_n^> - \mathcal{K}_m^<$ within which the theoretical estimate of exact conductivity $\mathcal{K}$ must lie. For details

on the applications of the complementary variational principles, interested readers are referred to chapter 5 in the the book by Srivastava [1] and references therein.

1.2.3 Relaxation-Time Approaches

The difficulty in deriving an (approximate) expression for lattice thermal conductivity can be appreciated from the discussion provided in the previous two subsections. Relaxation-time approaches provide simple alternatives to the variational approaches for deriving expressions for the conductivity. In general, due to their inelastic nature, anharmonic phonon interactions are not amenable to a relaxation-time picture [11]. But for simplicity of understanding the problem it is useful to introduce the concept of anharmonic phonon relaxation time. Starting from the phonon Boltzmann equation, the quantity $-\partial n_{\mathbf{q}s}/\partial t|_{\text{scatt}}$ in Eq. (1.11), or $P\boldsymbol{\psi}$ in Eq. (1.12), can be expressed using the concept of a relaxation-time $\tau_{\mathbf{q}s}$ for a phonon in mode $\mathbf{q}s$. It is assumed that on application of a temperature gradient each phonon in mode $\mathbf{q}s$ transports heat during its lifetime (i.e., before it is annihilated due to scattering events). Important contributions to the theory of thermal conductivity based on relaxation-time approaches have been made, among others, by Debye [12], Klemens [13], Callaway [14], Simons [15], and Srivastava [1, 16].

The simplest of relaxation-time approaches is the so-called *single-mode relaxation-time* method. In this picture it is assumed that while phonons in mode $\mathbf{q}s$ have been driven out of their equilibrium distribution on application of a temperature gradient and transport heat for the duration of their lifetime $\tau_{\mathbf{q}s}$, phonons in all other modes remain in their thermal equilibrium. In the language of the previous subsection, this means that while $\psi_{\mathbf{q}s} \neq 0$, $\psi_{\mathbf{q}'s'} = 0$ for $\mathbf{q}'s' \neq \mathbf{q}s$. With this restriction we can represent the scattering operator P by its diagonal part only:

$$\sum_{\mathbf{q}'s'} P^{ss'}_{\mathbf{q}\mathbf{q}'} \psi^{s'}_{\mathbf{q}'} \simeq P^{ss}_{\mathbf{q}\mathbf{q}} \psi^{s}_{\mathbf{q}}. \tag{1.20}$$

This allows the right-hand side of the Boltzmann equation in Eqs. (1.11) and (1.12) to be simplified to

$$-\frac{\partial n_{\mathbf{q}s}}{\partial t}\bigg|_{\text{scatt}} = \frac{n_{\mathbf{q}s} - \bar{n}_{\mathbf{q}s}}{\tau_{\mathbf{q}s}} = \frac{\bar{n}_{\mathbf{q}s}(\bar{n}_{\mathbf{q}s}+1)\psi_{\mathbf{q}s}}{\tau_{\mathbf{q}s}} = P^{ss}_{\mathbf{q}\mathbf{q}} \psi^{s}_{\mathbf{q}}. \tag{1.21}$$

The single-mode relaxation-time $\tau_{\mathbf{q}s}$ is thus defined from the relation

$$\tau^{-1}_{\mathbf{q}s} = \frac{P^{ss}_{\mathbf{q}\mathbf{q}}}{\bar{n}_{\mathbf{q}s}(\bar{n}_{\mathbf{q}s}+1)}. \tag{1.22}$$

Using Eqs. (1.12) and (1.15), the single-mode relaxation-time expression for thermal conductivity $\mathcal{K}_{\text{smrt}}$ becomes

$$\mathcal{K}_{\text{smrt}} = \frac{\hbar^2}{3N_0\Omega k_{\text{B}}T^2}\sum_{\mathbf{q}s} c_s^2(\mathbf{q})\omega^2(\mathbf{q}s)\tau_{\mathbf{q}s}\bar{n}_{\mathbf{q}s}(\bar{n}_{\mathbf{q}s}+1). \tag{1.23}$$

This expression can be viewed as the kinetic theory result

$$\mathcal{K} = \frac{1}{3}C_{\text{v}}^{\text{sp}}\bar{c}^2\bar{\tau}, \tag{1.24}$$

with C_{v}^{sp} as the phonon specific heat (heat capacity per unit volume), $\bar{c}$ as average phonon speed, and $\bar{\tau}$ as average phonon relaxation time. The single-mode relaxation-time expression in Eq. (1.23) is sometimes known as the Debye conductivity expression, as it was first used by Debye [12].

A significant improvement over the single-mode relaxation-time approach was made by Callaway [14], who included the special role played by the momentum conservation in anharmonic phonon interaction. In the language of phonon-scattering operator P, the extra contribution to the phonon relaxation time over the single-mode result is that due to the off-diagonal part of the operator corresponding to the momentum-conserving normal (N) processes. The Callaway expression for the conductivity is of the form given in Eq. (1.23), but with the single-mode relaxation-time τ replaced by an *effective relaxation-time* τ_{C}

$$\tau_{\text{C}} = \tau(1+\beta_{\text{C}}/\tau_{\text{N}}), \tag{1.25}$$

where the parameter β_{C} is a function of the single-mode relaxation-time τ and a contribution τ_{N} from anharmonic N-processes. The resulting conductivity expression can be expressed as

$$\mathcal{K}_{\text{C}} = \mathcal{K}_{\text{smrt}} + \mathcal{K}_{N\text{-drift}}. \tag{1.26}$$

The contribution from the N-drift term can be significantly important for pure materials.

An attempt to incorporate the role of off-diagonal anharmonic momentum nonconserving (umklapp, or U) processes was made by Srivastava [16]. The resulting model conductivity expression is similar to the Callaway expression, but with τ_{C} replaced by τ_{S}, where

$$\tau_{\text{S}} = \tau_{\text{m}}(1+\beta_{\text{S}}\tau_{\text{N}}) \tag{1.27}$$

with β_{S} including the effect of τ_{m}. Here τ_{m} includes a modification of the single-mode relaxation-time τ arising from the contribution of U-processes to the off-diagonal part of the operator P. Clearly, $\tau_{\text{S}} = \tau_{\text{C}}$ in the absense of such an attempt (i.e., when $\tau_{\text{m}} = \tau$).

1.3 Phonon-Dispersion Relations

From the discussion in the previous section it is clear that whatever level of the theory of lattice thermal conductivity we decide to use, evaluation of $\mathcal{K}$ requires knowledge of phonon-dispersion relation $\omega = \omega(\mathbf{q}s)$, phonon relaxation-time $\tau(\mathbf{q}s)$, and a scheme for performing summation over phonon wave vectors $\mathbf{q}$ and polarization s of the expression in Eq. (1.23). Calculation of the phonon-dispersion relation is a research topic in its own right, known as lattice dynamics, and is beyond the scope of this chapter. Interested readers are referred to the books in Refs. [1, 17]. From a knowledge of $\omega(\mathbf{q}s)$ for a given polarization index s the sum over $\mathbf{q}$ can be replaced by an integral

$$\sum_{\mathbf{q}} \to \int g(\omega)\,\mathrm{d}\omega, \tag{1.28}$$

where $g(\omega)$ is the density of phonon states at the frequency ω. In general, the density of states is inversely proportional to the magnitude of the phonon group velocity

$$g(\omega) \propto \frac{1}{|\nabla_{\mathbf{q}}\omega|}. \tag{1.29}$$

For a proper calculation of the density of states $g(\omega)$ it is essential to obtain numerical values of the phonon-dispersion relation $\omega(\mathbf{q}s)$ for a large number of phonon wave vectors $\mathbf{q}$ within the irreducible part of the Brillouin zone of the solid under consideration. We will not, however, discuss this further in the present context.

With a view to restricting our discussion to high-thermal-conductivity materials, in this section we will examine the main features of the phonon-dispersion relation in diamond and aluminium nitride as examples of three-dimensional systems, graphite as an example of *quasi*–two-dimensional system, and carbon nanotubes as examples of *quasi*–one-dimensional systems. We will also present a simplified version of the dispersion relation and density of states of these systems within the continuum limit for crystal structure.

1.3.1 Three-Dimensional Materials

(i) *Diamond.* The diamond crystal structure can be constructed from a consideration of the face-centered cubic lattice and by assigning each lattice point two carbon atoms at a relative separation of $a(1/4, 1/4, 1/4)$ from each other, where a is the cubic lattice constant. The atomic positions of a solid with a closely related structure, the zincblende structure, within the conventional cubic unit cell of length a, is shown in Fig. 1.1. The diamond structure can be identified with the zincblende structure when the two basis atoms are of the same species.

The phonon-dispersion relation and the density of states for diamond are shown in Fig. 1.2. The dispersion results are plotted along the three principal

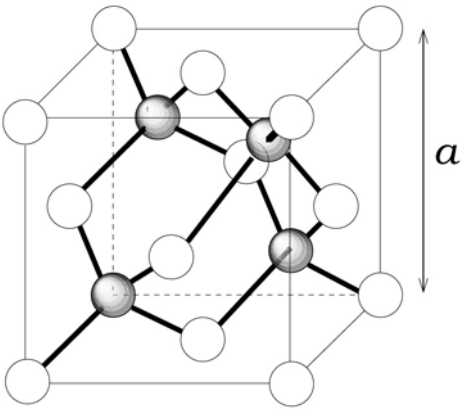

Fig. 1.1. Atomic positions in a solid with the zincblende structure, shown in the conventional cubic unit cell of size a.

symmetry directions: from Γ to X along [100], from Γ to K and extended up to X along [110], and from Γ to L along [111]. Due to two carbon atoms per primitive unit cell, there are six phonon branches. With increasing energy near the Brillouin zone center (Γ) these are the $\mathsf{T}_1\mathsf{A}$ (slow transverse acoustic), $\mathsf{T}_2\mathsf{A}$ (fast transverse acoustic), LA (longitudinal acoustic), $\mathsf{T}_2\mathsf{O}$ (fast transverse optical), $\mathsf{T}_1\mathsf{O}$ (slow transverse optical) and LO (longitudinal optical) branches. The density of states shows a few characteristic peaks, corresponding to flatness of the dispersion curves for the various polarization branches.

(ii) *β-AlN.* Aluminium nitride can assume two crystal phases: zincblende and wurtzite, known as β-AlN and α-AlN, respectively. In the zincblende

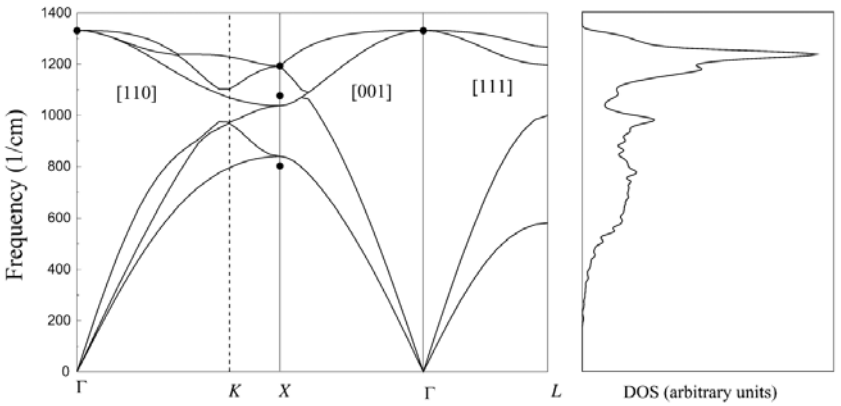

Fig. 1.2. Phonon-dispersion curves and density of states for diamond. The results are obtained from the application of a bond charge model [18]. Experimental measurements are indicated by filled circles.

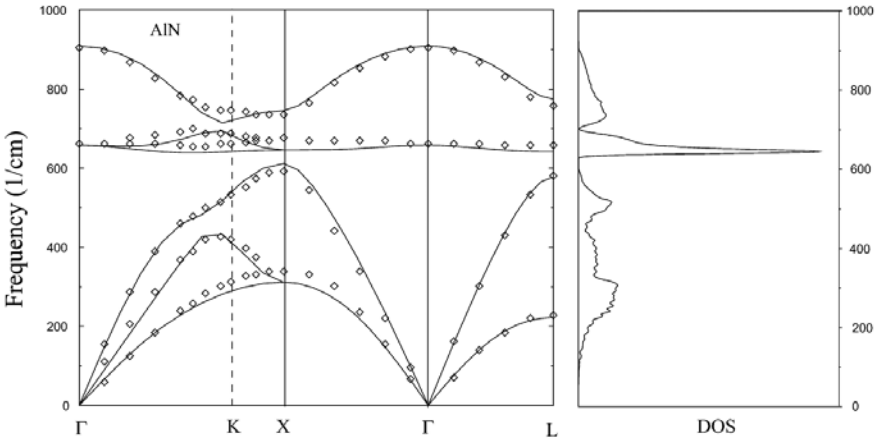

Fig. 1.3. Phonon-dispersion curves and density of states for AlN in the zincblende phase (β-AlN). Solid curves are obtained from calculations employing a bond charge model, and empty diamonds indicate experimental results. Taken from [19].

phase the cubic lattice constant is 4.38 Å. The phonon-dispersion curves for zincblende AlN, together with the density-of-states curve, are shown in Fig. 1.3. There are two significant differences between the dispersion curves for diamond and AlN. First, the TO branch in AlN is very flat, leading to a sharp peak in the density of states. Second, there is a large LO − TO splitting at the zone center (the Γ point) for AlN. This arises due to the ionic nature of AlN.

(iii) *α-AlN.* The crystal structure of the wurtzite phase of AlN can be constructed from the hexagonal lattice with a basis of four atoms such as: Al at $(0, 0, 0)$, $(2a/3, a/3, c/2)$ and N at $(0, 0, u)$, $(2a/3, a/3, c/2 + u)$. For α-AlN the hexagonal lattice constants are $a = 3.11$ Å and $c = \sqrt{(8/3)}a$, and the internal parameter is $u = 0.382$. Although each atom is tetrahedrally bonded to four neighbors of another species in both the zincblende and wurtzite structures, the connectivity of covalent bonds is different in the two structures. The crystal structure and the phonon-dispersion curves and the density of states for the α phase are shown in Figs. 1.4 and 1.5, respectively.

As a result of the geometrical differences between the β and α phases, there are a few differences in the phonon spectra and the density of states for the two phases. The four atoms within the wurtzite primitive unit cell result in three acoustic and nine optical branches. The lowest three optical branches are found to lie in the acoustic range obtained for the zincblende phase. The other six optical branches are well separated from the acoustic and the lower-lying optical branches. Thus there is an optical-optical gap in the phonon spectrum for α-AlN, as opposed to the optical-acoustic gap for β-AlN. This occurs because the extent of the Brillouin zone in the wurtzite phase along the [111] direction is only half of that in the zincblende phase. The density of

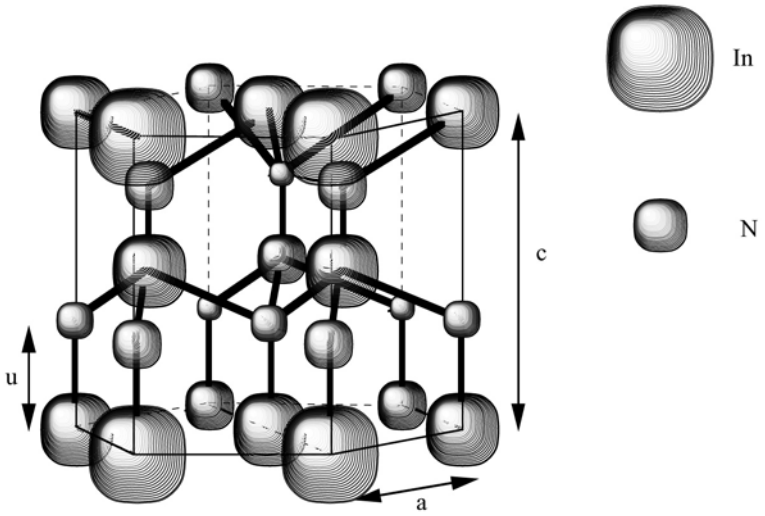

Fig. 1.4. Wurtzite crystal structure.

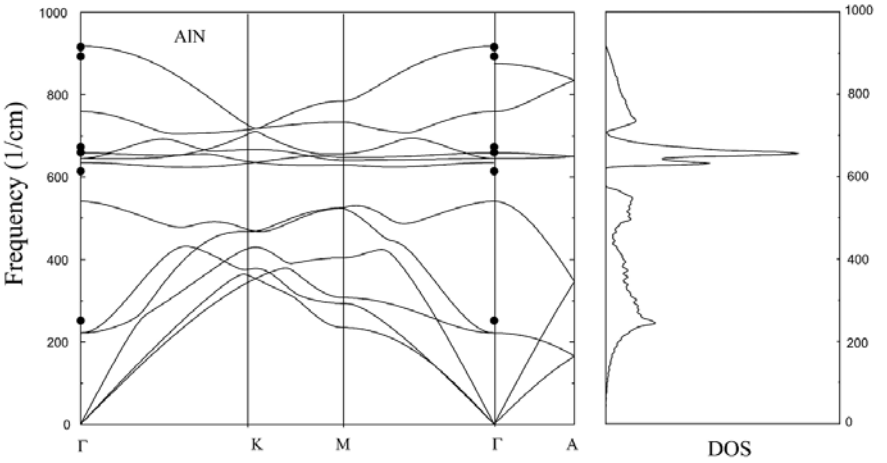

Fig. 1.5. Phonon-dispersion curves and density of states for AlN in the wurtzite phase (α-AlN). Solid curves are obtained from calculations employing a bond charge model, and filled circles indicate experimental results. Taken from [19].

states for α-AlN shows the development of a small but sharp peak just below the large peak in the lower part of the optical range for the zincblende phase.

1.3.2 Graphite, Graphene, and Nanotubes

(i) *Graphite.* The graphite structure is characterized by a basis of four carbon atoms assigned to each point of a simple hexagonal lattice. The distribution

of carbon atoms can be visualized in the form of atomic planes (the so-called basal planes). The basal atomic planes perpendicular to the c-axis have a honeycomb arrangement. The interplanar separation is 2.36 times the nearest-neighbor interatomic distance (1.42 Å) in a basal plane, indicating much weaker interlayer bonding.

The primitive translation vectors in a basal plane of graphite can be chosen as shown in Fig. 1.6. Corresponding to four atoms per primitive cell, there are 12 phonon branches for graphite, shown in Fig. 1.7. However, these branches are rather strangely ordered and show anomalous dispersion [20]. In a basal-plane direction there are three acoustic branches. While the LA and fast TA branches show normal dispersion, the slow TA branch (also called the bending mode branch) shows an anomalous dispersion $\omega \propto q^2$ for low q-values and a linear behavior $\omega \propto q$ for larger values of q. There is also a very low-lying TO branch at the zone center which shows a dispersion behavior similar to that of the slow TA branch. The frequencies of the in-plane TA, LA, and LO branches extend up to about 25 THz, 32 THz, and 47 THz, respectively. Along the interplanar direction the TA and LA branches are very low-lying (below $\nu_c(\mathrm{LA}) = (\omega_c(\mathrm{LA})/2\pi) \simeq 4$ THz) and get folded into dispersionless TO and LO branches, respectively.

(ii) *Graphene.* A single graphite plane is a graphene sheet. This hypothetical form of carbon, therefore, contains two carbon atoms per unit cell, leading to 6 phonon branches, as shown in Fig. 1.8(a) [21]. The three optical branches correspond to one out-of-plane mode and two in-plane modes. Near the zone center, with increasing energy the three acoustic branches correspond to an out-of-plane mode, an in-plane tangential (bond-bending) mode, and an in-plane radial (bond-stretching) mode, respectively. The out-of-plane (transverse) mode shows a q^2 dispersion, similar to that of the slow TA mode in graphite. The density of acoustic modes in the graphene sheet is a constant, as seen in Fig 1.8(b).

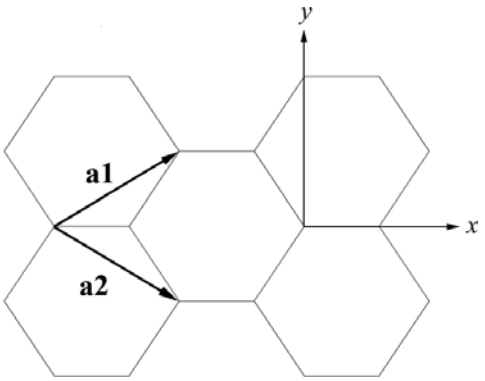

Fig. 1.6. The basal plane of graphite (i.e., a graphene sheet). The primitive translation vectors are indicated.

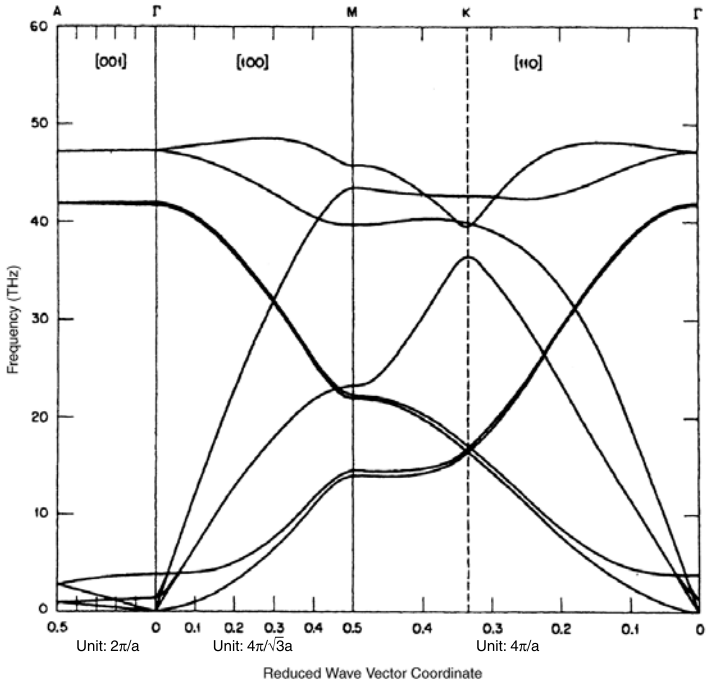

Fig. 1.7. Phonon-dispersion curves for the three-dimensional form of graphite. Taken from [20] with permission.

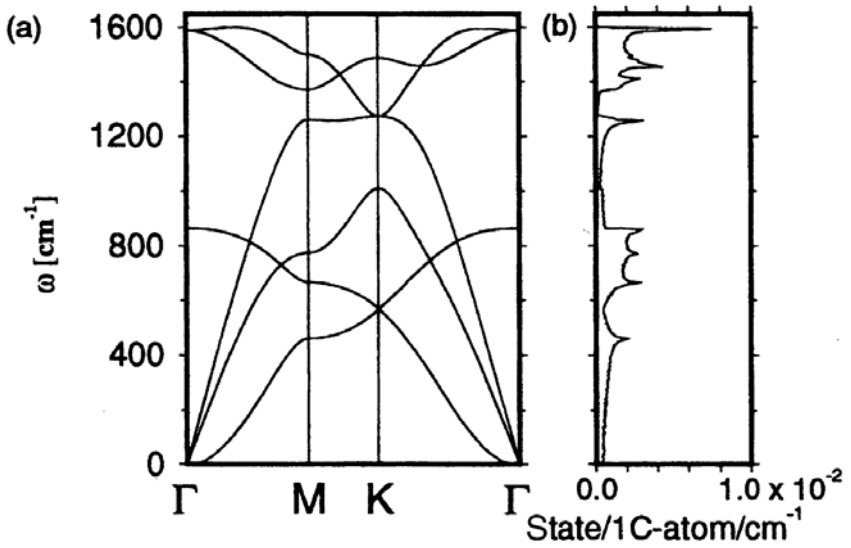

Fig. 1.8. (a) Phonon-dispersion curves and (b) density of states for a graphene sheet. Taken from [21] with permission.

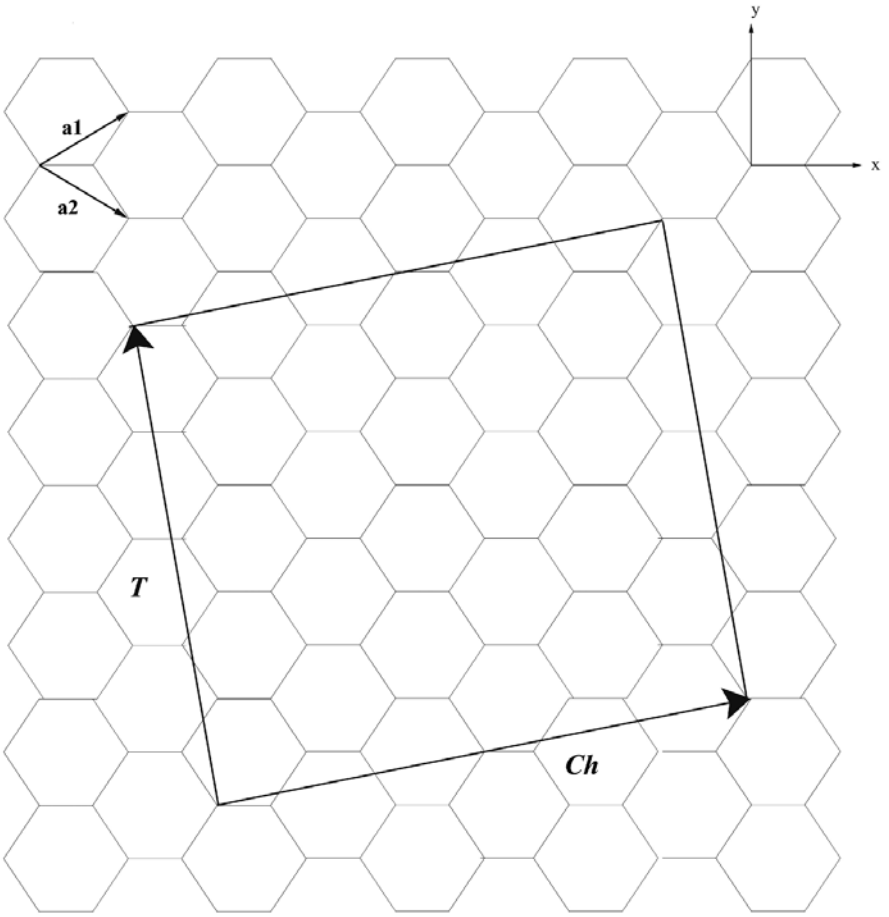

Fig. 1.9. A graphene layer and the unit cell of the (4,2) nanotube defined by the chiral vector $\mathbf{C}_h$ and the translation vector $\mathbf{T}$. There are 56 atoms in the nano-unit cell.

(iii) *Nanotubes.* A carbon nanotube is made by rolling up a graphene sheet. The structure of a single-wall nanotube can be specified by its chiral vector $\mathbf{C}_h$ and its translation vector $\mathbf{T}$. These vectors can be expressed as suitable linear combinations of the primitive translation vectors $\mathbf{a}_1$ and $\mathbf{a}_2$ of the graphene sheet. In particular, $\mathbf{C}_h = n\mathbf{a}_1 + m\mathbf{a}_2 \equiv (n, m)$. The diameter D of the tube is $D = |\mathbf{C}_h|/\pi$. An armchair nanotube corresponds to $\mathbf{C}_h = (n, n)$. The lattice translation vector parallel to the tube axis $\mathbf{T}$ is normal to the chiral vector $\mathbf{C}_h$: $\mathbf{C}_h \cdot \mathbf{T} = 0$. Fig. 1.9 shows the $\mathbf{C}_h$ and $\mathbf{T}$ vectors for the (4,2) nanotube.

Figure 1.10 shows the phonon-dispersion curves and the density of states for the (10,10) carbon nanotube [21]. There are 40 carbon atoms in the unit cell for the (10,10) nanotube, giving rise to 120 phonon branches. In accordance